C60 superstructure and carbide formation on the Al-terminated Al9Co2(001) surface

J. Ledieu, É. Gaudry, M.-C. De Weerd, P. Gille, R. D. Diehl, V. Fournée

C_{60} superstructure and carbide formation on the Al-terminated $Al_9Co_2(001)$ surface

J. Ledieu,[1,*] É. Gaudry,[1] M.-C. de Weerd,[1] P. Gille,[2] R. D. Diehl,[3] and V. Fournée[1]

[1]*Institut Jean Lamour (UMR7198 CNRS-Université de Lorraine), Parc de Saurupt, 54011 Nancy Cedex, France*

[2]*Department of Earth and Environmental Sciences, Crystallography Section, LMU, Theresienstr. 41, D-80333 München, Germany*

[3]*Department of Physics, Penn State University, University Park, Pennsylvania 16802, USA*

(Received 6 February 2015; published 17 April 2015)

We report the formation of an ordered C_{60} monolayer on the $Al_9Co_2(001)$ surface using scanning tunneling microscopy (STM), low-energy electron diffraction (LEED), x-ray and ultraviolet photoelectron spectroscopy (XPS/UPS), and *ab initio* calculations. Dosing fullerenes at 300 K results in a disordered overlayer. However, the adsorption of C_{60} with the sample held between 573–673 K leads to a [4, −2|1,3] phase. The growth of C_{60} proceeds with the formation of two domains which are mirror symmetric with respect to the [100] direction. Within each domain, the superstructure unit cell contains six molecules and this implies an area per fullerene equal to 91 Å^2. The molecules exhibit two types of contrast (bright and dim) which are bias dependent. The adsorption energies and preferred molecular configuration at several possible adsorption sites have been determined theoretically. These calculations lead to a possible scheme describing the configuration of each C_{60} in the observed superstructure. Several defects (vacancies, protrusions, . . .) and domain boundaries observed in the film are also discussed. If the sample temperature is higher than 693 K when dosing, impinging C_{60} molecules dissociate at the surface, hence leading to the formation of a carbide film as observed by STM and LEED measurements. The formation of Al_4C_3 domains and the molecular dissociation are confirmed by XPS/UPS measurements acquired at different stages of the experiment. The cluster substructure present at the $Al_9Co_2(001)$ surface dictates the carbide domain orientations.

DOI: 10.1103/PhysRevB.91.155418 PACS number(s): 68.35.bd, 68.37.Ef, 71.15.Mb, 71.20.Be

I. INTRODUCTION

The discovery of buckminsterfullerene (C_{60}) represents unquestionably a milestone for nanotechnology and more generally for physics and chemistry at the nanoscale [1]. With "the third man" of the carbon allotropic family unveiled [2], it was soon realized that C_{60} and its derivatives exhibited interesting tribological [3] and electronic properties including, for instance, superconductivity [4,5], insulating behavior in solid-state fullerenes [6] at high pressures [7], and even their potential use as active elements for electronic components [8,9]. Most of these properties are dictated by intermolecular and/or substrate-molecule bonding interactions.

While fullerene-based applications remain limited up to now, C_{60} is regarded today as an ideal prototypical molecule to determine molecule-substrate interfacial properties and to discover new surface phenomena. Likewise, using scanning tunneling microscopy (STM) technique in spectroscopic mode, the conductance of oriented molecules has been shown to vary depending on the C_{60}-substrate orientation [10]. This variation is attributed to differences in the charge transfer between molecule and surface with various interface geometries. This work emphasizes once more the need to investigate and determine the molecule-substrate bonding character, geometry, and mutual orientations in views of designing molecular electronics.

To this end, the growth of C_{60} molecules has been extensively studied on several close-packed metal surfaces [11]. Among the different systems under scrutiny, unusual and complex features have been reported for fullerene adsorption on Au(111) and Ag(111) surfaces [12–20]. Recently, Xie *et al.* have reported the formation of magic number C_{60}-Au complexes stabilized by a globalized metal-organic coordination mechanism [21]. It is thought that such process could inspire further studies aiming to design arrays of magnetic quantum dot for spin applications. Other surface phenomena have been outlined upon C_{60} adsorption on noble-metal surfaces. For instance, the adsorption of C_{60} on Ag(111) and Au(111) surfaces leads to the formation of surface vacancies which are then occupied by the fullerenes [22]. Molecules adsorb in two states; in vacancy and in top sites with different orientations, respectively [15–20]. This vacancy-adatom mechanism appears to be the rule rather than the exception, even for close-packed noble-metal surfaces. Moreover, diffusion of these surface vacancies below the monolayer occurs and results in a dynamic equilibrium of the C_{60} on Ag(111) and Au(111) surfaces. The molecules can then switch between the two states at a temperature-dependent rate. This dynamical behavior is reflected in STM images with molecule contrasts flipping from bright to dim and vice versa. In turn, these highly mobile vacancies beneath the monolayer can be regarded as a melting of the interfacial metal layer within a temperature range well below their normal melting temperatures [20]. Such dynamical phenomena have not been observed on low-index Al surfaces where the bonding is considered predominantly of covalent type. Three different phases have been so far reported consisting of pseudo-$c(4 \times 4)$ C_{60}/Al(110), $(2\sqrt{3} \times 2\sqrt{3})R30°C_{60}$/Al(111), and $(6 \times 6)C_{60}$/Al(111) structures [23–26]. Apart from an XPD study reported by Fasel *et al.* [27] where no surface reconstruction was considered, the characterization of C_{60} molecules on an Al(100) surface using STM, low-energy electron diffraction (LEED), and *ab initio* techniques is still lacking. Similarly, to our knowledge, fullerene adsorption on Al-terminated surfaces of binary systems has not been reported up to now.

*Corresponding author: julian.ledieu@univ-lorraine.fr

In this paper, we investigate the structure of C_{60} films formed on the $Al_9Co_2(001)$ surface as well as the adsorption configuration and the bonding character of the molecules at different adsorption sites. This intermetallic compound is also referred as a complex metallic alloy (CMA), although its unit cell is relatively small [28]. The Al_9Co_2 system is periodic, containing 22 atoms per unit cell, and its topmost surface layer consists of a slightly puckered pure Al layer [29]. To a first approximation, the local atomic arrangements resemble those found on the Al(100) surface. The situation becomes more complex when considering the subsurface layer, which contains both Al and Co atoms. It is important to note that the Al-Al bonding within the topmost $Al_9Co_2(001)$ surface layer presents a covalent character. In addition, the electronic structure of the surface layer is characterized by a reduction of the density of states at the Fermi level referred as a pseudogap. Because of its *quasi*square local atomic arrangement, this intermetallic offers the opportunity to study molecular adsorption on an "Al(100)-like" surface with a modified electronic structure. It would also serve to establish how much the covalent interactions present at the template surface limit or not surface reconstruction upon molecular adsorption.

The structural complexity associated with CMA surfaces (including quasicrystals as the ultimate case of complexity) results in surfaces with complex potential energy landscapes and consequently with a greater variety of adsorption sites than close-packed low-index Al surfaces for instance. As demonstrated by recent works on aperiodic systems [30,31], it is possible to take advantages of preferential adsorption sites to form molecular thin films with complex structures and potentially with unique physical properties. Thus, the Al_9Co_2 system represents an ideal playground to discover new surface phenomena with a complexity in-between "low-index elemental aluminium" and quasicrystal surfaces.

After a description of the methods in Sec. II, the fullerene superstructure reported in this paper will be presented in Sec. III along with the formation of a carbide structure. Adsorption geometries and energies of C_{60} molecules on possible adsorption sites on the $Al_9Co_2(001)$ surface will be presented in Sec. IV. These results, leading to a possible determination of the superstructure, will be discussed and compared to previous works on Al surfaces in Sec. V before we present the conclusions in Sec. VI.

II. METHODS

A. Experimental details

The Al_9Co_2 single crystal is an intermetallic compound grown using the Czochralski technique from an Al-rich solution. The $Al_9Co_2(001)$ surface preparation consists of cycles of Ar^+ ion sputtering for 30 min followed by annealing to 953 K for 90 min. The temperature is measured using an infrared optical pyrometer with an emissivity set to 0.35. Further details on the crystal growth and surface characteristics can be found in Ref. [29]. Prior to the adsorption experiment, the cleanliness and the composition of the surface is checked using x-ray photoelectron spectroscopy (XPS). The overall quality and the structure of the surface is monitored using STM and low-energy electron diffraction. The electronic structure of the clean surface is also measured by ultraviolet photoelectron spectroscopy (UPS). Adsorption of fullerenes is achieved by a dosing system which consists of tungsten wire (0.025 mm) tightly twisted around a glass tube. A K-type thermocouple is sealed into the pyrex tube and sticks in among the C_{60} molecules (fullerene powder, sublimed, 99.9 +%, Alfa Aesar). While dosing, several sample temperatures have been used, ranging from 300 to 1078 K. Throughout the experiment, the doser temperature has been set to 493 K with a fixed substrate-source distance of about 5 cm. A monolayer equivalent (1 MLE) is defined here by calculating the area covered by C_{60} molecules as a fraction of the overall image area with the $Al_9Co_2(001)$ surface held at 583 K. All measurements have been taken at room temperature.

B. Calculation details

Complementary to the experimental study, we performed density functional theory (DFT) calculations using the plane-wave Vienna *ab initio* simulation package (VASP) [32–35]. The interaction between the valence electrons and the ionic core is described using the projector-augmented wave (PAW) method [36,37] and the calculations are performed within the generalized gradient approximation (GGA-PBE) [38,39]. To account for van der Waals interactions, we used dispersion-corrected Kohn-Sham DFT energy functionals, where the conventional Kohn-Sham DFT energy functional is corrected by the DFT-D2 method [40]. Total-energy calculations were realized using a cutoff energy (E_{cut}) equal to 450 eV and a k-points grid set to $3 \times 3 \times 1$.

The surface was modeled with a seven-layer-thick asymmetric slab built by bulk truncation. The slab is made of four fixed atomic layers at the bottom and three atomic layers allowed to relax. The termination is a pure Al plane, in agreement with our previous study [29]. A 3×3 surface unit cell has been selected to ensure a small coverage and to minimize interactions between "isolated" molecules (the distance between two molecules is around 18.5 Å). The slab contains 341 atoms with a distance between two slab images equal to $\simeq$30 Å.

The adsorption energies are determined by the evaluation of the total-energy difference between the system $\{C_{60}$ on $Al_9Co_2(001)\}$ and the sum of the systems $\{C_{60}\}$ and $\{Al_9Co_2(001)\}$.

III. RESULTS

A. C_{60} superstructure

After annealing the sample to 953 K, the LEED pattern obtained on the clean $Al_9Co_2(001)$ surface [see Fig. 1 (inset)] exhibits sharp diffraction spots with a rectangular unit mesh. It has been shown that the $Al_9Co_2(001)$ surface is bulk terminated with Al-rich planes as topmost surface layers [29]. The surface unit mesh parameters are in agreement with those reported by Boström *et al.* [41] for the monoclinic bulk model [a = 6.2163 Å, b = 6.2883 Å (90°)]. Upon the initial adsorption of C_{60} molecules, the LEED pattern starts to degrade and finally vanishes for 1 MLE coverage. Contrary to what is occurring on Al(110) and (111) surfaces, the mobility of C_{60} molecules on

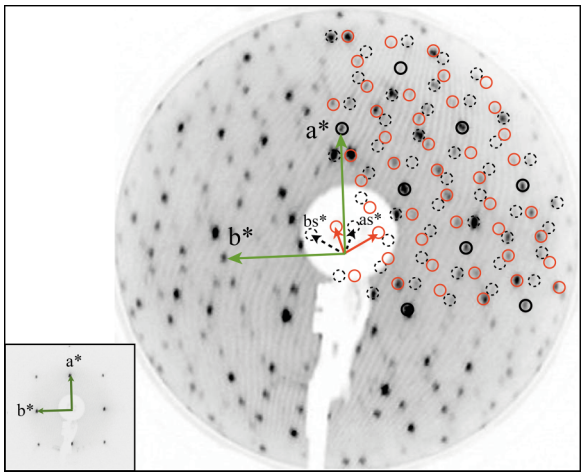

FIG. 1. (Color online) LEED pattern recorded at 26 eV after dosing 1.3 MLE C_{60} with the sample held at 613 K. The reciprocal lattice vectors as* and bs* are represented by the small arrows (dashed line). Inset: LEED pattern (26 eV) recorded on the clean $Al_9Co_2(001)$ surface after annealing to 953 K.

the $Al_9Co_2(001)$ surface is limited at 300 K and a disordered layer is obtained (also observed for C_{60}/quasicrystal systems at 300 K [42]). A new LEED pattern is observed when the sample is held between 573 and 673 K while dosing or after room-temperature deposition. This temperature range is above the multilayer desorption temperature. Figure 1 presents the LEED pattern obtained while dosing 1.3 MLE C_{60} molecules with the sample held at 613 K. The diffraction pattern consists of two domains that are mirror symmetric with respect to the *a* axis of the clean surface. The superstructure, which is commensurate with the clean surface, is described by the following matrix notation:

$$Al_9Co_2(001) - \begin{bmatrix} 4 & -2 \\ 1 & 3 \end{bmatrix} - 6C_{60}.$$

The growth mode of the superstructure has been monitored using STM by incremental depositions with the sample held at 643 K. For each domain, the lattice parameters and angle of the superstructure unit cell are equal to $a_s = 27.87$ Å, $b_s = 19.86$ Å with $\phi = 98.6^\circ$. The growth of the molecular film proceeds with the initial decoration of the terrace step edges [Fig. 2(a)]. This preferential adsorption initiates the formation of dense islands which grow laterally across terraces with impinging molecules. In some cases and for higher coverage, island nucleation can start on the lower side of terrace step edges. The islands will usually be faceted with a larger sharp edge at $\pm 72^\circ$ with respect to the [100] direction, orientation alternating on consecutive terraces. Using higher magnification and for higher coverage, the formation of an ordered monolayer of fullerenes is confirmed. The STM measurements [see Fig. 2(b)] reveal the presence of two C_{60} domains as expected from LEED analysis and the initial island growth morphology. At this stage, the resolution is sufficient to confirm also the domain orientations with respect to the underneath clean substrate [see uncovered surface area in the central top part of Fig. 2(b)]. Figure 2(c) presents an almost defect-free region of one C_{60} domain. The fullerenes are well

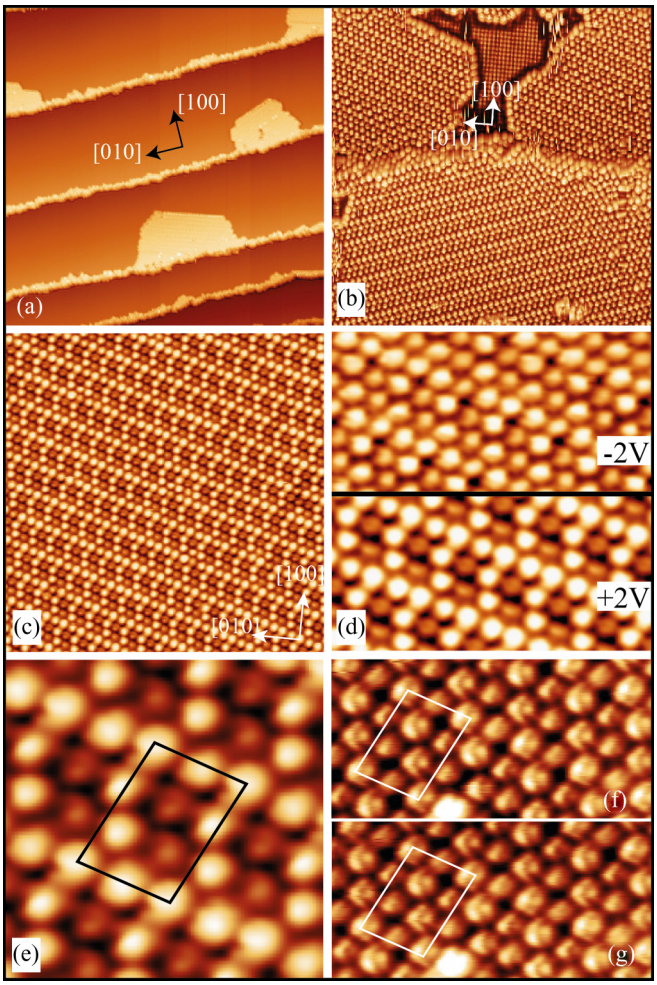

FIG. 2. (Color online) (a) 200 nm × 200 nm high-resolution STM image indicating that growth proceeds via step edge decoration with 0.15 MLE C_{60} ($V_b = +2.0$ V; $I_t = 0.57$ nA). (b) 46 nm × 46 nm STM image for 0.65 MLE C_{60} coverage ($V_b = +1.5$ V; $I_t = 0.10$ nA). (c) 32 nm × 32 nm high-resolution STM image for 1.3 MLE C_{60} coverage ($V_b = +2.0$ V; $I_t = 0.09$ nA). (d) 12 nm × 12 nm high-resolution STM of the dosed surface where the line indicates a change in the bias polarity ($I_t = 0.09$ nA). (e) 6 nm× 6 nm high-resolution STM image highlighting one unit cell. (f), (g) 10 nm × 5 nm STM image of the same region recorded several minutes apart. The bright defect is used as a reference point to directly compare the two images and one unit cell has been highlighted ($V_b = -2.0$ V; $I_t = 0.2$ nA).

ordered and display a bright and a dim contrast. Over the time of investigation, there were no dynamics associated with the bright and dim contrasts at 300 K. The calculated fast Fourier transform (FFT not shown here) of a single domain reveals an oblique unit cell with dimensions matching those extracted from the LEED pattern. As shown in Fig. 2(d), the contrast of the fullerenes is bias dependent. The dim molecules at +2 V are now the brightest at −2 V. For positive bias (+2 V), the bright to dim height difference is measured at about 1.2 Å and this apparent height difference is inverted and reduced to about 0.5 Å at negative bias.

The unit cell shown in Fig. 2(e) is composed of six C_{60} molecules (two dim and four bright) which lead to an area per fullerene equal to 91 Å^2 compared to 87 Å^2 for a perfectly hexagonal close-packed layer (C_{60}-C_{60} distance taken as

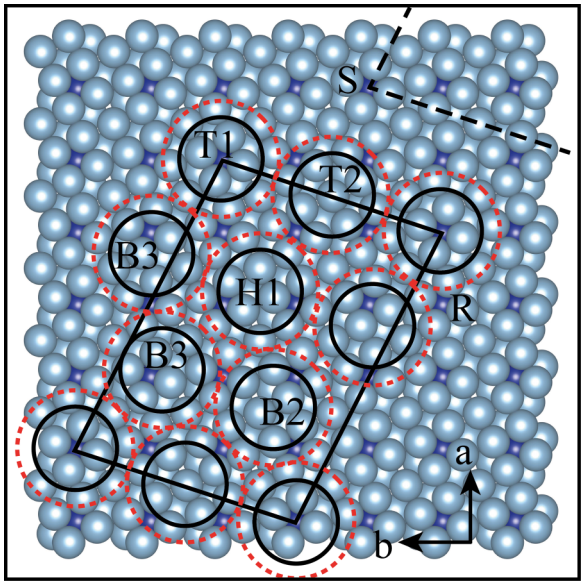

FIG. 3. (Color online) Model representing the C_{60} molecules and the underneath substrate. The circles correspond to the cage diameter (full line) and van der Waals radius (dashed line) of the fullerenes. The dark and light blue/gray spheres are, respectively, the Co and Al atoms of the substrate. The full (*R*) and dashed (*S*) lines are examples of equivalent ways to place the superstructure unit cell above the clean surface while keeping their vertices decorated by the *S*-1 Co atoms.

10 Å). On several images, the molecules display some internal structure which indicates that they do not rotate on the surface, i.e., their position is locked at 300 K. Consequently, the internal structure for each molecule is identical on images recorded minutes apart [see Figs. 2(f) and 2(g)]. From the LEED and STM analysis, it is now possible to visualize how the C_{60} monolayer is positioned above the substrate. To this end, a model is presented in Fig. 3 where the superstructure unit cell and the substrate lattice parameters have been outlined. The cage diameter of 7.1 Å (full circle) and the van der Waals radius of 10 Å (dashed line) of the fullerenes drawn at scale are superimposed on top of the $Al_9Co_2(001)$ surface (*S*). As it will be demonstrated later on using *ab initio* calculations, it is reasonable to position the overlayer in such a way that one of the C_{60} molecule sits on top of Co subsurface atoms (*S*-1) of the $Al_9Co_2(001)$ surface. This is also the site used arbitrarily to define the origin of the unit mesh. The presence of two domains of fullerenes originates from the atomic structure of the clean $Al_9Co_2(001)$ surface. Indeed, the $Al_9Co_2(001)$ surface is bulk terminated by pure Al layers. These terminations are separated by a single step height equal to half the *c*-lattice parameter. These surface terminations are related to each other by a 2_1 screw axis along *b* or by a glide operation along the *c* axis (reflection in an *ac* plane and a translation of half a unit cell in the c^* direction [43]). This leads to the formation of two C_{60} domains related to each other by a reflection operation. Here, the measurements do not allow us to associate the two superstructure unit-cell orientations to each of the two possible surface terminations.

Using XPS, the Al 2*p* and C 1*s* and Co 2*p* (not shown here) core levels have been monitored prior and after C_{60}

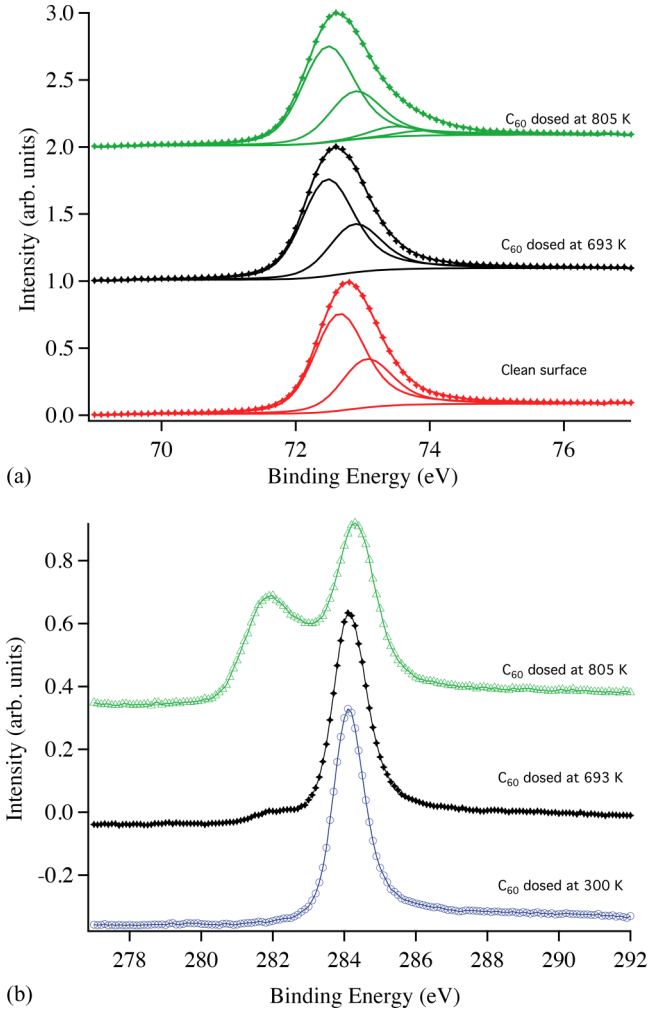

FIG. 4. (Color online) (a) Spectra of the Al 2*p* core level for the clean surface (bottom) and after 0.5-ML deposition with the sample held at 693 K (middle) and 805 K (top). (b) Spectra of the C 1*s* core level after 0.5-ML deposition at room temperature (bottom) and with the sample held at 693 K (middle), and at 805 K for 1 MLE deposition (top).

adsorption for various sample temperatures. With a Shirley background selected, the Al 2*p* spectra have been fitted using Doniach-Šunjić (DS) profile and Gaussian-Lorentzian line shapes [DS(α,*n*)SGL(*m*) [44]]. The Co 2*p* core levels are not altered regardless of the fullerene adsorption condition. As demonstrated in Fig. 4(a) (see bottom and middle spectra), the Al 2*p* spectra are identical in shape and width before and after deposition at 693 K. However, a chemical shift of 0.18 eV to lower binding energy is observed after C_{60} deposition. The C 1*s* core level has a binding energy of 284.1 eV after deposition at 300 K. Upon adsorption at higher temperature, the overall peak remains unchanged and an extra small component appears at about 282 eV [see Fig. 4(b)]. As it will be discussed later, molecular adsorption with the sample held above 693 K changes considerably the Al and C core-level spectra [top spectra of Figs. 4(a) and 4(b)].

The electronic structure of the deposited film has been investigated using UPS. The valence band spectra in Fig. 5(a) correspond to a coverage of 0.5 MLE C_{60} dosed at 300 and

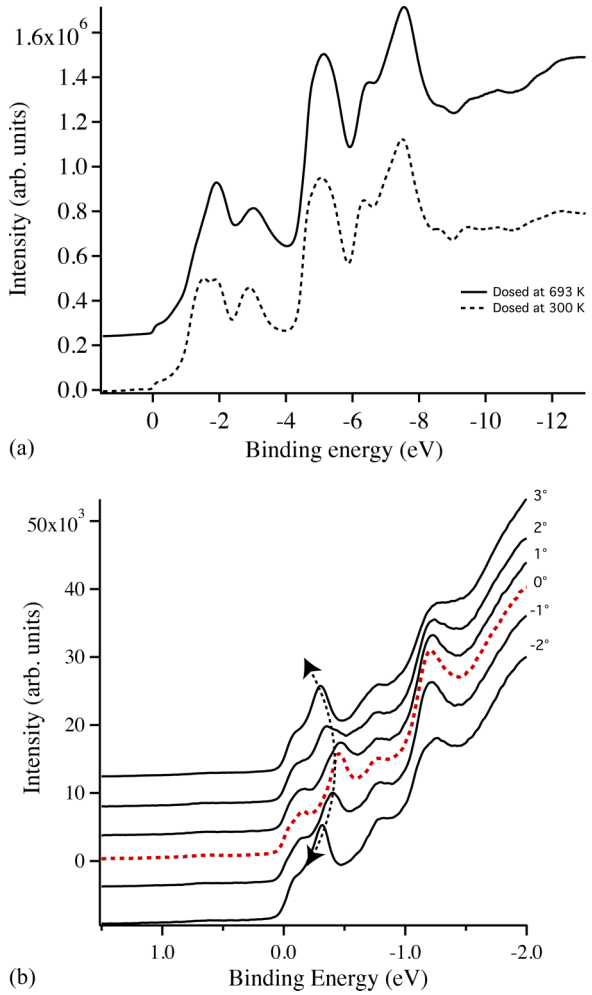

FIG. 5. (Color online) (a) UPS spectra after deposition of 0.5 MLE C_{60} with the sample held at 300 K (bottom) and 693 K (top). (b) UPS spectra for different takeoff angle obtained after deposition of 0.5 MLE C_{60} with the sample held at 805 K.

693 K (bottom and top spectrum, respectively). The different peaks observed between 0 and 12 eV are associated to the different molecular orbitals, the closest one to the Fermi level (E_F) corresponding to the highest occupied molecular orbital (HOMO). The presence of these peaks in the valence band indicates that the molecules stay intact at the surface upon adsorption under these dosing conditions. For 0.5 MLE C_{60} coverage, the contribution from the Co *d* states of the clean surface to the spectra is still important in the range 1 to 2 eV below E_F. The main difference between the spectra shown in Fig. 5(a) lies in the vicinity of the HOMO peak. When adsorption of C_{60} is performed at 300 K, there is a clear splitting of the HOMO peak. While the doublet vanishes for higher deposition temperatures, the HOMO peak remains broad with a clear shoulder at about 1.2 eV attributed this time to a contribution of Co *d* states (see Fig. 3 in Ref. [29]). When comparing both spectra, there is a small shift of 0.1 eV of the molecular orbitals (HOMO-1, HOMO-2, . . .) to higher binding energy for the film prepared at 693 K. Interestingly, the position of the HOMO peak is not altered (no shift) between both preparation conditions.

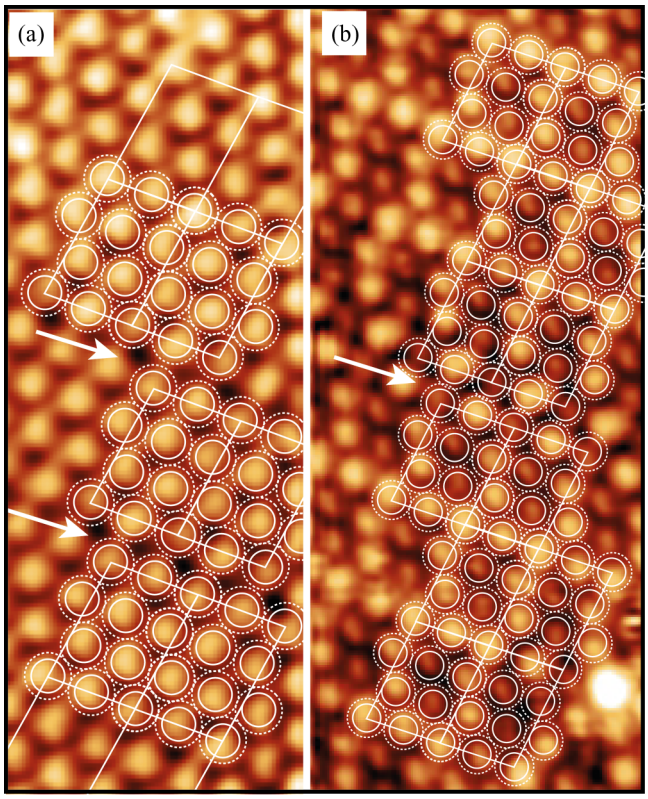

FIG. 6. (Color online) High-resolution STM images of the dosed surface with (a) 16 nm × 6 nm ($V_b = -2.5$ V; $I_t = 0.17$ nA) and (b) 19 nm × 8 nm ($V_b = +2.5$ V; $I_t = 0.07$ nA). The arrows indicate the domain boundaries.

B. Defects and domain boundaries

Although well ordered, several point defects (vacancies, protrusions, ...) and domain boundaries have been identified within the C_{60} monolayer. On Fig. 2(c), for instance, there are several molecules (middle right of the STM image) which do not exhibit the expected contrast within the superstructure unit cell (dim instead of bright). Regarding the domain boundary, several configurations have been observed across terraces and two examples with identical interface arrangements (see Fig. 6) have been selected to illustrate this point. To understand the local arrangement, the superstructure unit cells decorated with C_{60} are superimposed on the STM images. In Fig. 6(a), the arrows point towards two domain walls separated by a width equal to a whole superstructure unit cell. In this configuration, the intermolecular separation at both domain interfaces is between 9.86 and 9.93 Å. In Fig. 6(b), only one domain boundary is present (see the arrow). It is interesting to note that the molecular contrast along the short edge of the overlayer unit cell is alternating between bright and dim at the interface. Scenarios that can explain such interface arrangements will be discussed in Sec. V.

In Fig. 3, the superstructure unit cell has been represented twice: once as a full line (*R*) and another as a dashed line (*S*). In both cases, the superstructure unit cell is positioned identically with respect to the substrate unit cell and this leads to identical STM image contrasts. When adjacent unit cells are not in registry (here the *R* and *S* configurations in Fig. 3),

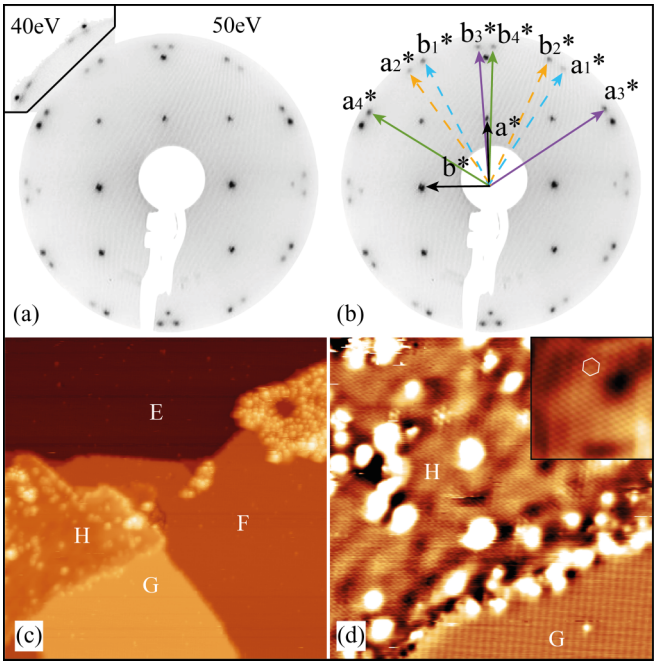

FIG. 7. (Color online) (a), (b) LEED pattern obtained at 50 eV for 0.5 MLE deposition at 300 K followed by annealing to 713 K. Inset: LEED pattern (40 eV) recorded after annealing 1.3 MLE to 966 K. (c) 85 nm × 85 nm high-resolution STM image for 0.5 MLE with the sample held at 805 K. (d) 27 nm × 27 nm high-resolution STM image showing both the clean $Al_9Co_2(001)$ surface (G) and the new phase (H). Inset: 6 nm × 6 nm STM image (FFT filtered) of a region from image (d) revealing the hexagonal structure.

then it results in the domain boundaries presented in Fig. 6. The adlayer-substrate positioning has been chosen following the *ab initio* calculations which will be presented in Sec. IV.

C. Aluminium carbide formation

In this section, we report an additional phase which can be formed either by post-annealing or directly dosing 1 MLE C_{60} above 693 K. The LEED pattern shown in Fig. 7(a) has been obtained for 0.5 MLE deposited at 300 K and annealed to 713 K. It consists of sharp diffraction spots originating from the clean substrate along with an additional 24 new spots on the outer part of the LEED pattern. Only 16 of them are clearly distinguishable as the other 8 spots coincide with some of the (1 × 1) LEED pattern. The LEED pattern is now best described by two sets [dashed and full reciprocal lattice vectors in Fig. 7(b)] of two domains, each set being mirror symmetric with respect to the a axis. For the two domains defined by $\vec{a}_1 * /\vec{b}_1 *$ and $\vec{a}_2 * /\vec{b}_2 *$, the (0,1) first-order spots are in coincidence with the (2,1)/(2,−1) spots of the clean surface, respectively. For the two domains defined by $\vec{a}_3 * /\vec{b}_3 *$ and $\vec{a}_4 * /\vec{b}_4 *$, the (1,−1) first-order spots are in coincidence with the (−1,−2)/(−1,2) spots of the clean surface, respectively. Additional coincidence can be found for each domain. Consequently, the lattice parameters measured for the four hexagonal domains are equal to $\vec{b}_{1,2} = 3.22$ Å and $\vec{a}_{3,4} = \vec{b}_{3,4} = 3.24$ Å with $\phi = 120°$. The $\vec{a}_1$ and $\vec{a}_2$ have a value always slightly larger than $\vec{b}_1$ and $\vec{b}_2$, respectively, i.e., getting closer to 3.3 Å.

As demonstrated in the inset of Fig. 7(a), the LEED pattern is modified when the adsorption of 1.3 MLE C_{60} is carried out with a sample temperature set to 966 K. The 24 spots observed previously are still present but none of them coincide with those of the substrate. This is clearly visible in the inset where the (0,1) spot of the new phase is slightly off the (2,1) diffraction spot of the clean substrate. Furthermore, one can distinguish a very faint diffraction ring close to the edge of the LEED pattern passing through all 24 additional spots [partly visible in the inset of Fig. 7(a)]. This ring indicates the existence of many hexagonal domains with identical lattice parameters and randomly orientated azimuthally with respect to the substrate. From a careful analysis of the LEED pattern, the lattice parameters for the four well-defined hexagonal domains (and others forming the ring) are in this case equal to $a_i = b_i = 3.34 \pm 0.10$ Å (with $i = 1 \ldots 4$) and $\phi = 120°$.

The coexistence of the clean structure and the new phase is confirmed using STM. In Fig. 7(c), the terraces labeled E, F, and G correspond to the clean $Al_9Co_2(001)$ surface and the region H is associated with one domain of the hexagonal surface net. The height histogram calculated from the STM image indicates that the step heights between E-F and F-G is equal to 4.27 Å as expected for consecutive terraces of the clean surface. The step height between F and H is measured at 1.52 Å. In addition to this extra phase, STM images reveal remaining disordered C_{60} islands across terraces within which a limited amount of local hexagonal arrangements of fullerenes are distinguishable. A higher magnification of regions H and G is shown in Fig. 7(d). Here, the STM resolution is sufficient to identify the clean surface unit cell and the hexagonal unit mesh of the new phase [see inset of Fig. 7(d)]. The latter presents several defects (adatoms . . .) and is more corrugated than the $Al_9Co_2(001)$ surface. The FFT calculated from region H (not shown) indicates a lattice parameter equal to 3.35±0.15 Å for the new phase. Due to the accuracy of the measurements, the orientation and the dimension of the hexagonal unit mesh are in agreement with the domains described in the LEED patterns measured for the system annealed at 713 and at 966 K.

The formation of this new phase results in important changes in the Al 2p and C 1s core-level spectra. Extra features centered at 73.65 eV emerge in the Al 2p core-level spectrum, hence leading to a overall broadening of the line shape. Similarly, additional components appear in the C 1s spectrum towards lower binding energy (peak around 282 eV). It is important to note also a small shift (0.2 eV) of the most intense C1s component towards higher binding energy (284.3 eV). The overall shape (mainly the intensity of the components at ∼282 and ∼284 eV) of the C 1s core-level spectrum has been seen to change drastically with the fullerene coverage, annealing temperature and time.

The electronic structure is also considerably altered with the growth of the hexagonal phase. Spectra recorded up to 12 eV (not shown here) demonstrate that the spectral intensities of molecular orbitals (HOMO, HOMO-1, . . .) identified in Fig. 5(a) are drastically reduced. In Fig. 5(b), near E_F UPS valence band spectra have been collected for different takeoff angles. The red/dashed spectrum corresponds to normal emission with respect to the sample surface. The peak located

TABLE I. Adsorption energies (E_{ads}, eV), shortest C-Al distance ($d_{C\text{-}Al}$, Å) and relative height (Δz, Å) for a C_{60} molecule adsorbed on $Al_9Co_2(001)$.

Site	E_{ads} (eV)	$d_{C\text{-}Al}$ (Å)	Δz (Å)
T1	−3.18	2.10	0.11
T2	−2.16	2.19	0.22
T3	−1.95	2.15	0.26
H1	−2.72	2.11	0.07
B1	−2.58	2.06	0.48
B2	−2.78	2.15	0.00
B3	−2.92	2.10	0.44
B1b	−2.07	2.18	0.47
B2b	−2.53	2.18	0.27
B3b	−2.18	2.12	0.36
Tpent	−2.11	2.29	0.28

at −1.2 eV below E_F is associated with the Co d states of the clean surface. It can be seen that the peak positions remain unchanged with varying takeoff angles except for dispersive features observed between E_F and −0.5 eV.

IV. THEORETICAL RESULTS

A. Adsorption energies and geometries

As depicted in Table I and Fig. 8, different geometries are considered for the adsorption: top sites (T1–T3 and Tpent), bridge sites (B1–B3, B1b–B3b), and hollow sites (H1). The C_{60} molecule is positioned with either one hexagonal ring facing the surface (top sites T1–T3, hollow site H1), or with one C-C 6:6 bond along one Al-Al bond, in order to ensure symmetry matching between the molecule and the topmost layer. One configuration has been tested with the pentagonal ring of the C_{60} molecule facing the surface at the T1 site (Tpent site). The resulting adsorption energies and geometries are given in Table I and Fig. 8.

There is no clear correlation between the shortest C-Al distance or the molecule-surface distance and the adsorption energies, leading to the conclusion that electronic effects play an important role in the adsorption process. This is also well illustrated by the comparison of the H1 and T1 adsorption sites. The adsorption energy difference between these two sites ($\simeq$0.5 eV) cannot be interpreted by geometric effects as molecule-surface distance and adsorption geometry are similar. It may be due to the presence of subsurface Co atom (S-1) located below the center of the hexagonal ring facing the surface.

The C_{60} molecule remains almost intact on the surface, although small distortions have been identified. One can notice that the distances ($d_{C\text{-}G}$) between the center of mass of the C_{60} molecule (G) and the carbon atoms (C) are within ±0.05 Å of the corresponding distance in the free C_{60} molecule ($d^{free}_{C\text{-}G}$). The C-G distance out of this range involve C atoms close to the surface. For example, in the case of the T1 adsorption site, the four carbon atoms [see Fig. 9 (T1)] out of the $d^{free}_{C\text{-}G}$ ± 0.05 Å range are those involved in the C-Al bonding at the $Al_9Co_2(001)$ surface. This holds also for the four (resp. three) carbon atoms in the case of the H1 (resp. B3) adsorption sites [Fig. 9 (H1,B3)].

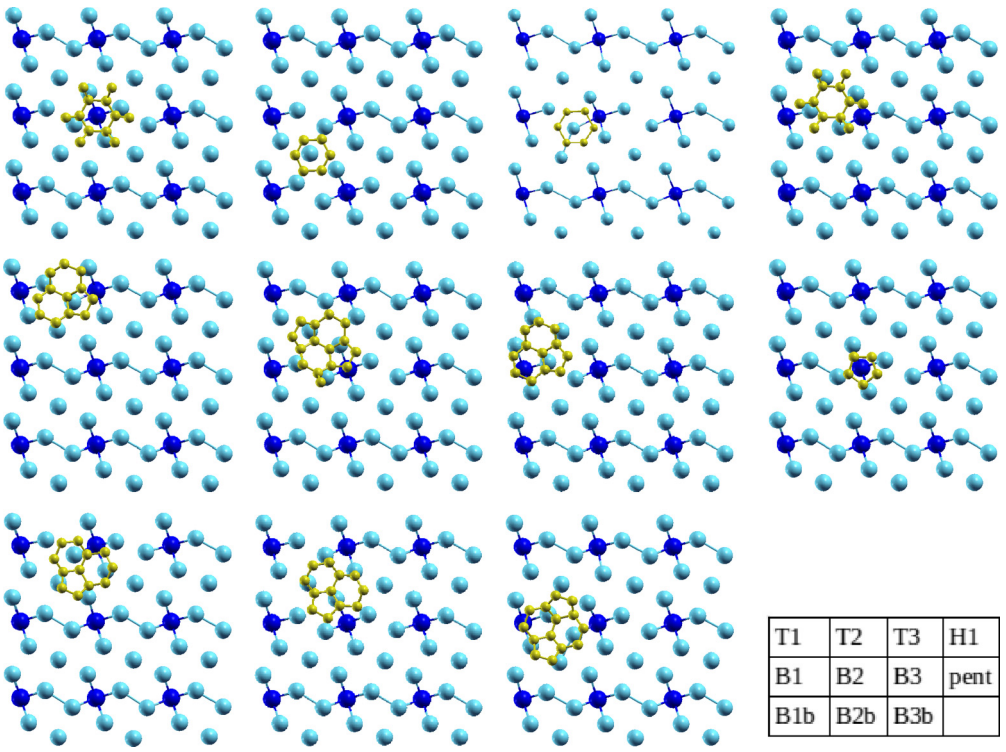

FIG. 8. (Color online) Adsorption geometries (top view) for a C_{60} molecule adsorbed on $Al_9Co_2(001)$. The topmost surface layer (pure Al plane), the subsurface Co atoms (S-1), and the C atoms at the bottom of the molecule are represented by medium (light blue), large (dark blue), and small (yellow) spheres, respectively.

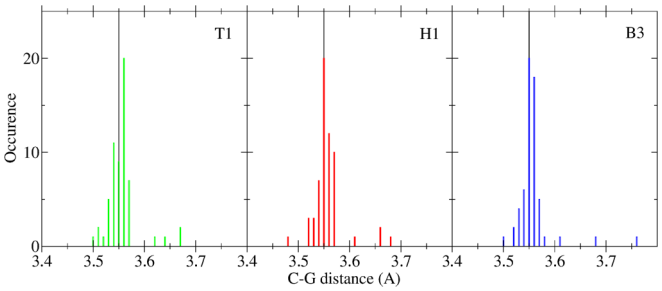

FIG. 9. (Color online) Histogram of C-G distances between carbon atoms (C) and the center of mass of the C_{60} molecule (G) in Å. The vertical straight line (gray) at 3.55 Å indicates the corresponding distance in the free C_{60} molecule.

B. Molecule-surface bonding

To get further insights into the molecule-surface bonding, the charge differences $\rho[C_{60}$ on $Al_9Co_2(001)] - \{\rho(\text{free } C_{60}) + \rho[Al_9Co_2(001)]\}$ have been calculated for a few adsorption sites. As shown in Figs. 10 and 11, the calculations highlight a wide variety of bonding geometries: a two-center bond between two adjacent carbon atoms of C_{60} and two surface Al atoms (B1, Fig. 11), a three-center bond between three carbon atoms belonging to a hexagonal ring of the C_{60} molecule and three surface Al atoms (B3, Fig. 11), a four-center bonding between four carbon atoms belonging to a hexagonal ring of the C_{60} molecule and four surface Al atoms (T1 and H1, Fig. 10), or more complex molecule-surface interactions (B2 and B2b, Fig. 11).

From the calculations, it appears that the adsorption energy scales with the number of Al-C bondings between the C_{60} molecule and the surface. This observation applies, for instance, between T1 and B3 sites having respectively four- and three-center bonds with an adsorption energy difference of $\simeq 0.25$ eV. This latter value is much lower than the typical energy one would expect for a single ionic or covalent bond. Hence, it implies a reorganization of the electronic distribution among the bonds with the increasing/decreasing number of Al-C bonds in order to stabilize the C_{60} molecules on different sites.

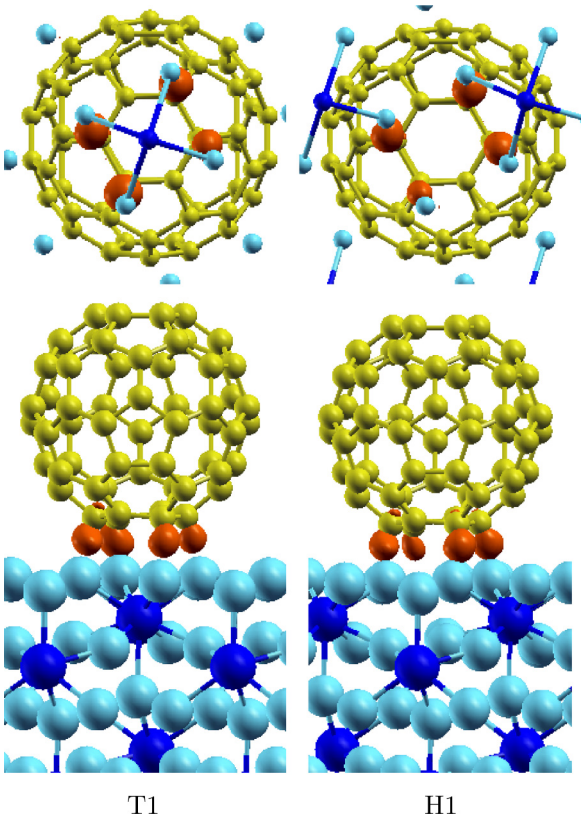

FIG. 10. (Color online) Isosurface of the charge differences $\rho[C_{60}$ on $Al_9Co_2(001)] - \{\rho(\text{free } C_{60}) + \rho[Al_9Co_2(001)]\}$ for the T1 and H1 sites (top and side views). The atomic radius on the top view is reduced to better identify the charge transfer.

C. Superstructure and vacancy

The four most stable adsorption sites are T1 (−3.18 eV), B3 (−2.92 eV), B2 (−2.78 eV), and H1 (−2.72 eV). The tiling of $Al_9Co_2(001)$ surface with C_{60} molecules based only on these four sites is incomplete and it requires an additional site occupation. This corresponds to the T2 site (Fig. 3) which is a slightly less stable adsorption site ($E_{ads} = -2.16$ eV). The molecule is then located on top of a surface Al atom.

Since C_{60} molecules deposited on metallic surfaces are generally adsorbed on surface vacancies, the adsorption energy of C_{60} adsorbed on a vacancy has been also calculated here. From the above tiling and the calculated adsorption energy, the vacancy has been created on T2 site by removing the central Al atom. The corresponding adsorption energy is −2.91 eV for this new configuration (C_{60} vacancy), i.e., in the energy range of the most stable adsorption sites determined previously (T1, H1, B2, B3). The energy required to create such a surface vacancy is $E^{N-1}_{slab} - E^{N}_{slab} + \mu_{Al}$. This leads to a value of about 1 eV by approximating the aluminium chemical potential in Al_9Co_2 to bulk aluminium one (−3.50 eV). This value is much lower than those calculated for bulk vacancies, which range from 1.50 to 2.10 eV depending on the vacancy position. Consequently, the C_{60} molecule on top of a surface vacancy is closer to the surface (relative height $\Delta z = -0.42$ Å) and presents shorter Al-C distances (2.10 Å) compared to the initial one calculated in Table I.

V. DISCUSSION

At 300 K, C_{60} molecules are mobile on the Al(110) and Al(111) substrates, leading to ordered monolayers [23–26]. The $Al_9Co_2(001)$ topmost surface layer consists of a pure buckled Al plane with a lateral density of 0.128 atom/Å^2, intermediate between the Al(110) and the close-packed Al(111) surfaces. Hence, the reduced mobility cannot be related to the lateral surface density but should be a consequence of a stronger molecule-substrate interactions in the case of the $Al_9Co_2(001)$ surface compared to Al(110) and Al(111) substrates and/or due to a larger corrugation of the surface potential energy in the case of the CMA surface. As seen in Fig. 5(b) (bottom curve), the signature of the disordered layer is the presence of a double peak between 1.4 and 2 eV below E_F. The origin of this doublet could be a splitting of the HOMO orbitals (∼0.3 eV apart) into two components by

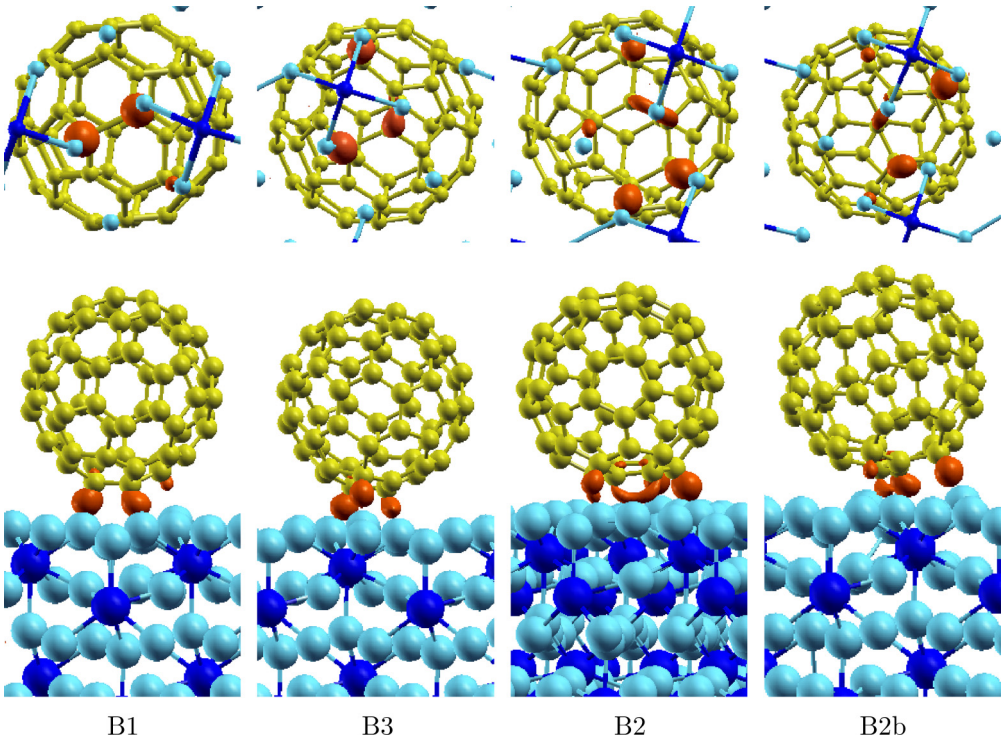

FIG. 11. (Color online) Isosurface of the charge differences $\rho[C_{60}$ on $Al_9Co_2(001)] - \{\rho(\text{free } C_{60}) + \rho[Al_9Co_2(001)]\}$ for few bridge sites (top and side views). The atomic radius on the top view is reduced to better identify the charge transfer.

symmetry-breaking interaction with the surface as previously reported for the C_{60}/Al(110) system [26].

An alternative explanation has been proposed by Schiessling *et al.* where intramolecular electronic correlations could lead to the band splitting observed for the C_{60}/Al(110) system [45]. At this submonolayer coverage, part of the clean $Al_9Co_2(001)$ surface is still uncovered. However, the maximum of the first peak (−1.55 eV) does not match the position of the Co *d* states. In addition, a similar doublet should have been observed for the ordered film [top spectrum of Fig. 5(a)] if it were arising from Co *d* states. Hence, we believe that the observed doublet originates from a splitting of the HOMO into two components.

A. Superstructure

To overcome the diffusion barrier resulting in an ordered monolayer, thermal energy must be provided either to the system *a posteriori* (annealing the deposited film) or to the sample during adsorption. A similar phenomenon has been reported for other Al-based complex metallic alloy surfaces (fivefold Al-Pd-Mn, fivefold Al-Cu-Fe, tenfold Al-Ni-Co, and tenfold Al-Cu-Co quasicrystals) [30,31]. On the fivefold Al-Pd-Mn quasicrystal surface, C_{60} adsorption at low coverage shows evidence of adsorbate local order within fivefold hollow sites at 300 K. These local correlations do not extend over larger regions with increasing coverage [46]. However, fullerene adsorption on quasicrystalline substrates at higher temperature leads to self-assembled molecular films with long-range quasiperiodic order [30,31]. Due to symmetry matching between the molecules (pentagonal face down) and the substrate, specific adsorption sites (hollow sites and white flowers) with local fivefold symmetry are preferentially decorated [31].

While symmetry matching is commonly observed between the threefold axis of the molecule and metal surface [mostly (111) surfaces], the scenario is different in the superstructure reported here. The unit mesh parameters of the clean surface are larger than other low-index Al surfaces. However, the unit-cell decoration is such that the topmost surface layer can be described locally by *quasi*square motifs (see Fig. 3). The average row separations along the [210] and [1$\bar{2}$0] directions are equal to 2.81 and 2.83 Å, respectively. As a first approximation and by considering only the first plane, the $Al_9Co_2(001)$ topmost puckered layer presents the closest similarities with an Al(100) surface (lateral interatomic distance of 2.86 Å). Although several studies have been performed on the Al(110) and Al(111) surfaces, information remains scarce on the Al(100). Using x-ray photoelectron diffraction (XPD), it has been demonstrated that the adsorption of C_{60} on the Al(100) surface leads to a fourfold-symmetric pattern [27]. Combined with single-scattering cluster calculations, the results are consistent with fullerene adsorbed facing with a single edge atom towards the substrate with four different azimuthal orientations [27]. To maximize symmetry matching and *a priori* to lower the total energy of the system, some of the adsorbates within the [4,−2| 1,3] phase may adopt a similar adsorption geometry as on the Al(001) surface. The remaining molecules will present other orientations with hexagonal face down for instance. In Figs. 2(f) and 2(g), the STM images, although of limited resolution, reveal different internal structures of the molecules. This observation tends to confirm multiple orientations (both polar and azimuthal) of the fullerenes within the monolayer. This is further confirmed by

ab initio calculations, which demonstrate that both hexagonal ring facing the surface and C-C 6:6 bond along one Al-Al bond coexist within the superstructure. The molecule-surface configuration is therefore site dependent, most likely to accommodate for the topmost layer buckling somehow. Differences in the molecular orientations result in a variety of substrate-adsorbate bonding interactions and consequently to differences in charge transfers among adjacent fullerenes. This is particularly well illustrated when comparing charge transfers between B3 (three-center bond) and B2 adsorption sites in Fig. 11. These charge-transfer differences among fullerenes due to different adsorption configurations will impact the STM image contrast. This is indeed reflected in the intermolecular contrast variation (bright and dim) and in the bias dependency observed experimentally within the superstructure. Similarly, calculated STM images for several adsorption sites (not shown here) exhibit a variety of shapes and contrasts. At this stage, additional measurements using low-temperature STM would be required to compare simulated and experimental images and eventually to obtain more quantitative and meaningful information.

An alternative explanation for this contrast difference would be the formation of vacancies beneath dimmer adsorbed molecules. This interface reconstruction has been recently reported for C_{60} adsorption on noble metals (Au, Ag). These nanopits account for the bright/dim contrast of the adsorbate due to a real height difference [18–20,22]. In both systems, the monolayer displays a dynamical behavior with a flipping between bright/dim contrast. It has been shown that no dynamical behavior (no flipping between bright/dim contrast and no rotation) has been observed for C_{60} molecules adsorbed on the $Al_9Co_2(001)$ surface. This could be explained by the vacancy formation energy (site T2 only tested) being slightly larger than those calculated for Ag and Au(111) surfaces [20]. Moreover, the contrast within the superstructure unit cell is drastically modified depending on the bias applied (dim molecules becoming the brightest) which points towards an electronic effect rather than a physical height difference, which is still possible. Indeed, height differences exist for C_{60} molecules adsorbed on the T1, $T2^{vac}$, H1, B2 sites (closer to the surface, $\Delta z \leqslant 0.11$ Å) compared to the B3 adsorption site ($\Delta z = 0.44$ Å).

The adsorption of fullerenes leads also to a rearrangement of the substrate on the Al(111) surface. Indeed, a close-packed hexagonal layer of $2\sqrt{3} \times 2\sqrt{3}\ R30^\circ$ periodicity is transformed into a 6×6 phase as an interface reconstruction raises one third of C_{60} molecules [24]. This rearrangement is accompanied with an additional peak in the Al $2p$ core-level spectrum [23]. From a comparison between the Al core-level line shape prior and after the superstructure formation [see Fig. 4(a)], the spectra appear identical. In our case, the resolution may not be sufficient to ascertain the presence/absence of an extra component in the spectrum. However, it has to be mentioned that an extra peak is not observed for the C_{60}/Al(110) system [26]. One of the reasons for the lack of reconstruction may lie in the chemical bonding network present in the Al-Co compound. The bulk structure of the Al_9Co_2 system can be described by monocapped square antiprism clusters which are preserved intact up to the surface termination [29,47]. Several covalentlike interactions have been identified within these entities [48]. It leads to a nonuniform total charge density distribution resembling the cluster shape and consequently giving these geometric entities a real physical significance. Contrary to metallic bulk aluminum, it is possible that the covalent interaction present within the $Al_9Co_2(001)$ substrate will limit interface reconstruction upon molecular adsorption.

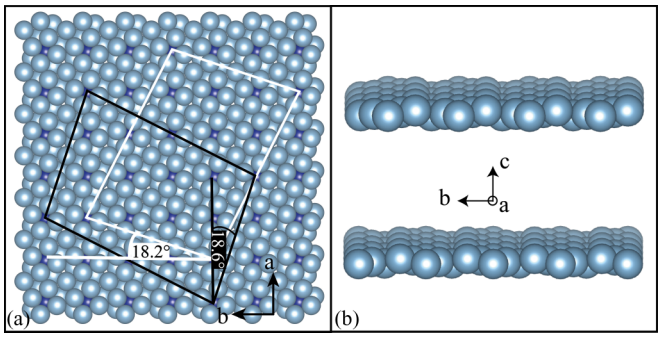

FIG. 12. (Color online) (a) The observed (white line) and hypothetical (black line) orientations of the superstructure unit cell are superimposed over one of the two possible $Al_9Co_2(001)$ surface terminations. (b) Three-dimensional representation (side view) of the two pure Al puckered planes appearing alternatively as topmost terminations on terraces. Note the arrangement and the buckling of these two layers along the b axis.

From the work reported by Maxwell *et al.* [26], the type of bonding between C_{60} molecules and Al surfaces is characterized as intermediate and predominantly covalent. For both Al(110) and Al(111) surfaces, the desorption temperature is estimated at 730 K. On the $Al_9Co_2(001)$ surface, the fullerenes decompose above 700 K which suggests a stronger site specificity on the intermetallic which leads to an increased reactivity of the C_{60} molecules on this surface, i.e., dissociation of the fullerene. It is also consistent with the need for thermal energy to order the monolayer at lower temperature. From the calculations, the molecule-substrate bonding is shown to be site specific with a strong influence of the underneath Co atoms. All configurations tested are stable and this is why one needs to perform the adsorption with the sample at high temperature to obtain an ordered molecular film. The calculated adsorption energies are significantly larger than those calculated for C_{60} on Au and Ag(111) surfaces.

Regarding the superstructure unit-cell dimensions, it results from the matching between the C_{60} molecules and the substrate lattice (commensurate overlayer). In the configuration presented in Fig. 3, the superstructure has 70 metal atoms per cell. The monolayer can be considered as a distorted hexagonal structure due to strong molecule-substrate interaction. As the a parameter is almost equal to b (respectively, 6.2163 and 6.2883 Å), it is not straightforward to understand the monolayer unit-cell orientation. Indeed, Fig. 12(a) reveals that there exists apparently an alternative way to position the superstructure unit cell while preserving the commensurability with the clean surface. The small edge length of this hypothetical superstructure orientation is then at 18.6° off the [100] direction and not at 18.2° off the [010] direction as it is currently experimentally observed. Underneath the molecules, the local atomic arrangement of the template would be apparently very similar for both orientations. Hence, it must

be down to a delicate balance between the plane buckling difference between [100] and [010] directions [see Fig. 12(b)] and *a fortiori* the molecule-substrate orientation, and the van der Waals (vdW) intermolecular interactions that favor one orientation. The superstructure unit cell is decorated by two and three C_{60} molecules along the small edge length (19.86 Å) and the diagonal (31.7 Å at 11.4° off the [100] direction) of the cell, respectively. This brings the average intermolecular separation of 9.93 and 10.57 Å in each case. A unit-cell orientation rotated by 90° (18.6° off the [100] direction) would have resulted to values of 9.84 and 10.69 Å. Between these two possibilities, the experimentally observed orientation leads to nearest-neighbor distances closer to the value reported for solid C_{60} molecules, i.e., a structure of reduced strain.

B. Domain boundaries

As presented in Fig. 6, domain boundaries have been identified within the ordered monolayer. Figure 2(a) demonstrates that domains nucleate at different locations along the step edges. Upon adsorption, islands will laterally extend until they reach another island. Depending on the registry between the islands, a domain boundary will emerge or not at the island interface. The two unit cells labeled *S* and *R* in Fig. 3 are positioned on equivalent sites leading to similar molecular contrast and model the domain boundaries presented in Fig. 6. At the sharp interfaces indicated by arrows in Fig. 6, the intermolecular distance is between 9.86 and 9.93 Å and C_{60} interacts via vdW interaction. These domain boundaries should not be considered as strain relief mechanism. They represent defects originating from the lateral growth of individual islands which are not in-registry with one another. Similarly, domain boundaries have been observed along the long edge length of the superstructure unit cell which is another possibility for island interfaces. At the domain boundary, the contrast of the molecules located at sites T1 and T2 alternates between bright and dim (see Fig. 6). This phenomenon is even more pronounced at positive bias. Away from this interface, the molecules positioned at T1 and T2 exhibit a bright contrast. A careful analysis of STM images recorded on the same region demonstrates that this contrast difference is unaffected at the boundary when using opposite bias. Several effects could explain the dim contrast observed ranging from charge transfer to local surface reconstruction. It is also possible that the dim molecules originate from the formation of surface vacancies. Additional calculations will be required to test this hypothesis and this is beyond the scope of this work.

C. Carbide formation

We now turn into the new phase observed at higher dosing or annealing temperature. The binding energies of the extra components in the C 1*s* and Al 2*p* core-level spectra [see top curves in Figs. 4(a) and 4(b)] and the lattice parameters of the new structure determined from LEED and STM measurements are consistent with the formation of a carbide thin film (Al_4C_3; trigonal crystal structure with $a = 3.34$ Å and $c = 24.97$ Å [49]). Here, it is not possible to determine the depth of the carbide phase, i.e., if the thickness is equivalent to one or more unit cell along the [001] directions or just one or few layers belonging to the carbide structure. The Co 2*p* core-level spectra remains unchanged upon adsorption. At the lowest formation temperature, two diffraction spots of each carbide domain are in coincidence with those of the template, which means a carbide lattice parameter reduced by about 3% in at least one direction depending on the domain. The carbide-substrate orientations are such that the [010] and [100] directions of the hexagonal phase are aligned, respectively, with the [210] and [$1\bar{2}0$] directions of the substrate (see Fig. 13). As explained above, the average row separations of the clean surface along the [210] and [$1\bar{2}0$] directions are equal to 2.81 and 2.83 Å, respectively. To optimize the substrate-film interface, the interatomic row separations (initially equal to 2.89 Å) of the carbide domains are slightly compressed along the [120] and [210] directions, respectively. In other words, the carbide film orientation is dictated by the orientation of the monocapped square antiprism clusters (*quasi*square motifs within the topmost layer) and do not follow the [100] and [010] directions of the substrate unit cell itself. Such impact of the elementary cluster on the domain orientation has already been reported for the $Cu/Al_{13}Co_4$ system [50].

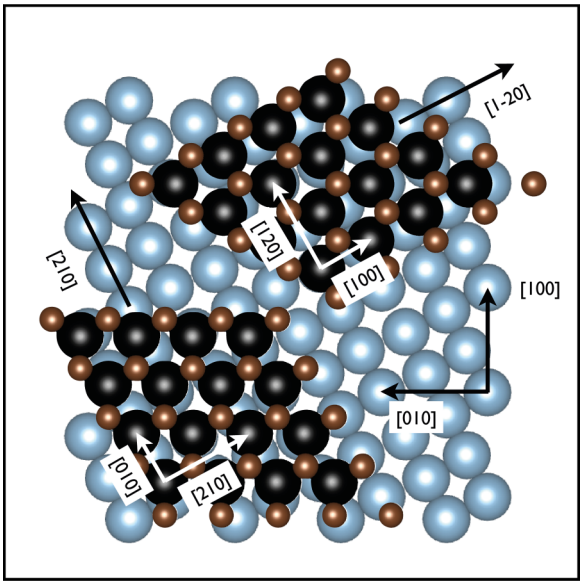

FIG. 13. (Color online) Schematic representation of the carbide-substrate orientation relationship. A single (001) bulk layer (arbitrary selection) of Al_4C_3 has been superimposed with two orientations on top of the Al-terminated layer of the Al_9Co_2(001) surface. The small spheres correspond to C atoms while the others to Al atoms [blue/gray = Al_9Co_2(001) surface; black = Al_4C_3].

When the temperature and the fullerene exposure are higher, the carbide film recovers its expected lattice parameters and additional domains randomly oriented appear. This translates by the absence of coincidence between film-substrate diffraction spots [see inset of Fig. 7(a)] and the appearance of a very faint ring in the LEED pattern. The dissociation of the fullerenes above 693 K is confirmed by UPS measurements with the disappearance of characteristics states of the fullerenes (HOMO, HOMO-1, ...). Finally, angle-resolved UPS measurements displayed in Fig. 5(b) demonstrate the presence of dispersive *sp* electronic states as expected for a carbide thin film, i.e., a parabolic free-electron-like density of states.

VI. CONCLUSIONS

The adsorption of C_{60} molecules has been characterized on the $Al_9Co_2(001)$ surface using STM, LEED, XPS, and UPS. A new superstructure is formed when the adsorption is performed either with the sample held between 573–673 K or by post-annealing the disordered film up to 673 K. The LEED pattern indicates the presence of two domains which are mirror symmetric with respect to the [100] direction. Photoemission measurements demonstrate that the fullerenes remain intact upon adsorption. The growth proceeds with the decoration of step edges, leading to different fullerene domains. Within the superstructure (six molecules per unit cell), the C_{60} molecules will display bright and dim contrast depending on the STM bias. The measurements demonstrate that the fullerenes do not rotate once ordered at the surface. It is thought that the chemical bonding network present within the Al_9Co_2 system will prevent/reduce interface reconstruction. *Ab initio* calculations indicate that C_{60} molecules adopt two main configurations within the superstructure: hexagonal ring facing the surface and C-C 6:6 bond along Al-Al bond in order to ensure symmetry matching between the molecule and the topmost layer. The C-Al bonding interactions are of covalent character. Several domain boundaries have been identified within the film and they originate from the interface between independently growing islands. Above 673 K, we observed the formation of four carbide domains also symmetric with respect to the [100] direction. Their respective orientation allows an optimization of the interatomic row spacing along the [120] and [210] directions of the trigonal system with the [210] and [1$\bar{2}$0] directions of the substrate. This carbide-template relationship results into a strained carbide film along specific directions. The monocapped square antiprism clusters present within the topmost substrate termination dictate those carbide orientations. The valence band is then characterized by dispersive *sp*-like derived electronic states.

ACKNOWLEDGMENTS

The Région Lorraine and CNRS (INCAS Project No. PICS05892) are acknowledged for their financial support. This work was granted access to the HPC (High Performance Computing) resources of the IDRIS under the Allocation No. 2015-096339 made by GENCI (Grand Equipement National de Calcul Intensif). Part of this work is a result of the cooperation within the European C-MAC.

[1] H. W. Kroto, J. R. Heath, S. C. O'Brien, R. F. Curl, and R. E. Smalley, Nature (London) **318**, 162 (1985).
[2] H. W. Kroto, Current Contents, PC&ES **33**, 8 (1993).
[3] Bharat Bhushan, B. K. Gupta, Garrett W. Van Cleef, Cindy Capp, and James V. Coe, Appl. Phys. Lett. **62**, 3253 (1993).
[4] A. F. Hebard, M. J. Rosseinsky, R. C. Haddon, D. W. Murphy, S. H. Glarum, T. T. M. Palstra, A. P. Ramirez, and A. R. Kortan, Nature (London) **350**, 600 (1991).
[5] R. M. Fleming, A. P. Ramirez, M. J. Rosseinsky, D. W. Murphy, R. C. Haddon, S. M. Zahurak, and A. V. Makhija, Nature (London) **352**, 787 (1991).
[6] W. Krätschmer, L. D. Lamb, K. Fostiropoulos, and D. R. Huffman, Nature (London) **347**, 354 (1990).
[7] M. N. Regueiro, P. Monceau, A. Rassat, P. Bernier, and A. Zahab, Nature (London) **354**, 289 (1991).
[8] R. C. Haddon, A. S. Perel, R. C. Morris, T. T. M. Palstra, A. F. Hebard, and R. M. Fleming, Appl. Phys. Lett. **67**, 121 (1995).
[9] A. Dodabalapur, H. E. Katz, L. Torsi, and R. C. Haddon, Science **269**, 1560 (1995).
[10] G. Schull, N. Néel, M. Becker, J. Kröger, and R. Berndt, New J. Phys. **10**, 065012 (2008).
[11] X.-Q. Shi, M. A. Van Hove, and R.-Q. Zhang, J. Mater Sci. **47**, 7341 (2012).
[12] Eric I. Altman and Richard J. Colton, Phys. Rev. B **48**, 18244 (1993).
[13] Eric I. Altman and Richard J. Colton, Surf. Sci. **295**, 13 (1993).
[14] Wei Chen, Hongliang Zhang, Han Huang, Lan Chen, and Andrew Thye Shen Wee, ACS Nano **2**, 693 (2008).
[15] J. A. Gardener, G. A. D. Briggs, and M. R. Castell, Phys. Rev. B **80**, 235434 (2009).
[16] T. Sakurai, X. D. Wang, T. Hashizume, V. Yurov, H. Shinohara, and H. W. Pickering, Appl. Surf. Sci. **87-88**, 405 (1995) (Proceedings of the 41st International Field Emission Symposium).
[17] Lin Tang, Yangchun Xie, and Quanmin Guo, J. Chem. Phys. **135**, 114702 (2011).
[18] K. Pussi, H. I. Li, Heekeun Shin, L. N. Serkovic Loli, A. K. Shukla, J. Ledieu, V. Fournée, L. L. Wang, S. Y. Su, K. E. Marino, M. V. Snyder, and R. D. Diehl, Phys. Rev. B **86**, 205406 (2012).
[19] H. I. Li, G. J. P. Abreu, A. K. Shukla, V. Fournée, J. Ledieu, L. N. Serkovic Loli, S. E. Rauterkus, M. V. Snyder, S. Y. Su, K. E. Marino, and R. D. Diehl, Phys. Rev. B **89**, 085428 (2014).
[20] H. Shin, A. Schwarze, R. D. Diehl, K. Pussi, A. Colombier, É. Gaudry, J. Ledieu, G. M. McGuirk, L. N. Serkovic Loli, V. Fournée, L. L. Wang, G. Schull, and R. Berndt, Phys. Rev. B **89**, 245428 (2014).
[21] Y.-C. Xie, L. Tang, and Q. Guo, Phys. Rev. Lett. **111**, 186101 (2013).
[22] H. I. Li, K. Pussi, K. J. Hanna, L.-L. Wang, D. D. Johnson, H.-P. Cheng, H. Shin, S. Curtarolo, W. Moritz, J. A. Smerdon, R. McGrath, and R. D. Diehl, Phys. Rev. Lett. **103**, 056101 (2009).
[23] A. J. Maxwell, P. A. Brühwiler, S. Andersson, D. Arvanitis, B. Hernnäs, O. Karis, D. C. Mancini, N. Mårtensson, S. M. Gray, M. K.-J. Johansson, and L. S. O. Johansson, Phys. Rev. B **52**, R5546 (1995).
[24] M. K.-J. Johansson, A. J. Maxwell, S. M. Gray, P. A. Brühwiler, D. C. Mancini, L. S. O. Johansson, and N. Mårtensson, Phys. Rev. B **54**, 13472 (1996).
[25] M. K.-J. Johansson, A. J. Maxwell, S. M. Gray, P. A. Brühwiler, and L. S. O. Johansson, Surf. Sci. **397**, 314 (1998).
[26] A. J. Maxwell, P. A. Brühwiler, D. Arvanitis, J. Hasselström, M. K.-J. Johansson, and N. Mårtensson, Phys. Rev. B **57**, 7312 (1998).
[27] R. Fasel, P. Aebi, R. G. Agostino, D. Naumović, J. Osterwalder, A. Santaniello, and L. Schlapbach, Phys. Rev. Lett. **76**, 4733 (1996).

[28] Julian Ledieu, Émilie Gaudry, and Vincent Fournée, Sci. Technol. Adv. Mater. **15**, 034802 (2014).
[29] S. Alarcón-Villaseca, J. Ledieu, L. Serkovic-Loli, M.-C. de Weerd, P. Gille, V. Fournée, J.-M. Dubois, and É. Gaudry, J. Phys. Chem. C **115**, 14922 (2011).
[30] J. A. Smerdon, K. M. Young, M. Lowe, S. S. Hars, T. P. Yadav, D. Hesp, V. R. Dhanak, A. P. Tsai, H. R. Sharma, and R. McGrath, Nano Lett. **14**, 1184 (2014).
[31] Vincent Fournée, Émilie Gaudry, Julian Ledieu, Marie-Cécile de Weerd, Dongmei Wu, and Thomas Lograsso, ACS Nano **8**, 3646 (2014).
[32] G. Kresse and J. Hafner, Phys. Rev. B **47**, 558 (1993).
[33] G. Kresse and J. Hafner, Phys. Rev. B **49**, 14251 (1994).
[34] G. Kresse and J. Furthmüller, Phys. Rev. B **54**, 11169 (1996).
[35] G. Kresse and J. Furthmüller, Comput. Mater. Sci. **6**, 15 (1996).
[36] P. E. Blöchl, Phys. Rev. B **50**, 17953 (1994).
[37] G. Kresse and D. Joubert, Phys. Rev. B **59**, 1758 (1999).
[38] J. P. Perdew, K. Burke, and M. Ernzerhof, Phys. Rev. Lett. **77**, 3865 (1996).
[39] J. P. Perdew, K. Burke, and M. Ernzerhof, Phys. Rev. Lett. **78**, 1396 (1997).
[40] S. Grimme, J. Comput. Chem. **27**, 1787 (2006).
[41] M. Boström, H. Rosner, Y. Prots, U. Burkhardt, and Y. Grin, Z. Anorg. Allg. Chem. **631**, 534 (2005).
[42] E. J. Cox, J. Ledieu, V. R. Dhanak, S. D. Barrett, C. J. Jenks, I. Fisher, and R. McGrath, Surf. Sci. **566-568**, 1200 (2004).
[43] The c^* axis is perpendicular to the (001) planes and 4.77° off the c axis.
[44] CasaXPS, Peak fitting in XPS (Casa Software Ltd, 2006), www.casaxps.com.
[45] J. Schiessling, M. Stener, T. Balasubramanian, L. Kjeldgaard, P. Decleva, J. Nordgren, and P. A. Brühwiller, J. Phys.: Condens. Matter **16**, L407 (2004).
[46] J. Ledieu, C. A. Muryn, G. Thornton, R. D. Diehl, D. W. Delaney, T. A. Lograsso, and R. McGrath, Surf. Sci. **472**, 89 (2000).
[47] Y. Grin, F. R. Wagner, M. Armbrüster, M. Kohout, A. Leithe-Jasper, U. Schwartz, U. Wedig, and H. G. von Schnering, J. Solid State Chem. **179**, 1707 (2006).
[48] G. Trambly de Laissardière, D. Nguyen-Manh, and D. Mayou, Prog. Mater. Sci. **50**, 679 (2005).
[49] T. M. Gesing and W. Jeitschko, Z. Naturfors. Sect. B, J. Chem. Sci. **50**, 196 (1995).
[50] R. Addou, A. K. Shukla, M.-C. de Weerd, P. Gille, R. Widmer, O. Gröning, V. Fournée, J.-M. Dubois, and J. Ledieu, J. Phys.: Condens. Matter **23**, 435009 (2011).